EUROPEAN ORGANIZATION FOR NUCLEAR RESEARCH

CERN-EP/90-20
February 15th, 1990

MEASUREMENT OF W AND Z PRODUCTION CROSS SECTIONS AT THE CERN $\bar{p}p$ COLLIDER

The UA2 Collaboration

Bern - Cambridge - CERN - Heidelberg - Milano -
Orsay (LAL) - Pavia - Perugia - Pisa - Saclay (CEN)

J.Alitti[10], R.Ansari[6], R.E.Ansorge[2], P.Bagnaia[3,a], P.Bareyre[10], G. Blaylock[3], P.Bonamy[10], M.Bonesini[5,3], C.N.Booth[3], K.Borer[1], D.Buskulic[6], G.Carboni[9], D.Cavalli[5], V.Cavasinni[9], P.Cenci[8], J.C.Chollet[6], C.Conta[7], G.Costa[5], F.Costantini[9,3], J.Crittenden[10], A.Dell'Acqua[7], B.DeLotto[7,b], T.DelPrete[9], R.S.DeWolf[2], L.DiLella[3], G.F.Egan[3,c], K.F.Einsweiler[3], L.Fayard[6], A.Federspiel[1], R.Ferrari[7], M.Fraternali[7,d], D.Froidevaux[6], G.Fumagalli[3,7], J.M.Gaillard[6], F.Gianotti[5], O.Gildemeister[3], C.Gössling[3,e], V.G.Goggi[7,3], S.Grünendahl[4], K.Hara[1,f], S.Hellman[3], E.Hugentobler[1], K.Hultqvist[3], E.Iacopini[9,g], J.Incandela[3], K.Jakobs[3], P.Jenni[3], E.E.Kluge[4], N.Kurz[4], S.Lami[4,9], P.Lariccia[8], M.Lefebvre[2,3], L.Linssen[3], B.Lisowski[3], M.Livan[7,h], P.Lubrano[3], C.Magneville[10], L.Mandelli[5], L.Mapelli[3], M.Mazzanti[5], K.Meier[3], B.Merkel[6], J.P.Meyer[10], M.Moniez[6], R.Moning[1], M.Morganti[9,i], L.Müller[1], D.J.Munday[2], C.Onions[3], T.Pal[3,1], M.A.Parker[3], G.Parrour[6], F.Pastore[7], E.Pennacchio[7], J.M.Pentney[2], M.Pepe[8], L.Perini[5,d], C.Petridou[9], P.Petroff[6], H.Plothow-Besch[4], G.Polesello[5,3], A.Poppleton[3], M.Punturo[8], L.Rasmussen[3], J.P.Repellin[6], A.Rimoldi[7], J.G.Rushbrooke[2,j], P.Scampoli[8], J.Schacher[1], S.L.Singh[2], S.Stapnes[3], A.V.Stirling[10], F.Tondini[9,8], S.N.Tovey[3,c], E.Tsesmelis[c], M.Valdata-Nappi[9,k], V.Vercesi[3,7], A.R.Weidberg[3], P.S.Wells[2], T.O.White[2], D.R.Wood[3], S.A.Wotton[2], H.Zaccone[10]

(submitted to Zeitschrift für Physik C)

Abstract

Results on the production cross sections of W and Z bosons detected in the UA2 experiment are given based on a large sample of $W \rightarrow e\nu$ and $Z \rightarrow e^+e^-$ decays. The measured cross sections are $\sigma_W^e = 660 \pm 15(\text{stat}) \pm 37(\text{syst})$ pb, $\sigma_Z^e = 70.4 \pm 5.5(\text{stat}) \pm 4.0(\text{syst})$ pb and their ratio $R = 9.38^{+0.82}_{-0.72}(\text{stat}) \pm 0.25(\text{syst})$. In the framework of the Standard Model, the measured value of R is used to determine the total width of the W, $\Gamma(W) = 2.30 \pm 0.19(\text{stat}) \pm 0.06(\text{syst})$ GeV.

1 Laboratorium für Hochenergiephysik, Universität Bern, Sidlerstraße 5, 3012 Bern, Switzerland
2 Cavendish Laboratory, University of Cambridge, Cambridge, CB3 0HE, UK
3 CERN, 1211 Geneva 23, Switzerland
4 Institut für Hochenergiephysik der Universität Heidelberg, Schröderstraße 90, 6900 Heidelberg, FRG
5 Dipartimento di Fisica dell'Università di Milano and Sezione INFN Milano, 20133 Milano, Italy
6 Laboratoire de l'Accélérateur Linéaire, Université de Paris-Sud, 91405 Orsay, France
7 Dipartimento di Fisica Nucleare e Teorica, Università di Pavia and INFN, Sezione di Pavia, Via Bassi 6, 27100 Pavia, Italy
8 Dipartimento di Fisica dell'Università di Perugia and INFN, Sezione di Perugia, via Pascoli, 06100 Perugia, Italy
9 Dipartimento di Fisica dell'Università di Pisa and INFN, Sezione di Pisa, Via Livornese, S.Piero a Grado, 56100 Pisa, Italy
10 Centre d'Etudes Nucléaires de Saclay, 91191 Gif-sur-Yvette Cedex, France
a) Now at Dipartimento di Fisica, Università di Roma, Italy
b) Now at Dipartimento di Fisica, Università di Udine, Italy
c) Visitor from the University of Melbourne, Parkville, Australia 3052
d) Now at Istituto di Fisica, Università di Palermo, Italy
e) Now at Institut für Physik, Universität Dortmund, FRG
f) Now at University of Tsukuba, Tsukuba, Ibaraki 305, Japan
g) Also at Scuola Normale Superiore, Pisa, Italy
h) Now at Dipartimento di Fisica, Università di Cagliari, Italy
i) Now at Dipartimento di Fisica e INFN di Bologna, Università Bologna, Italy
j) Now at Bond University, Gold Coast, Queensland, Australia 4217
k) Now at Dipartimento di Fisica dell'Università della Calabria e gruppo INFN, Cosenza, Italy

1. INTRODUCTION

Data taken at the CERN $\bar{p}p$ Collider in the period 1981-1985 were used by the UA1 [1] and UA2 [2] experiments to determine the production cross sections of the W and Z bosons. A data sample eight times larger, corresponding to an integrated luminosity of 7.8 pb^{-1} at a centre of mass energy $\sqrt{s} = 630$ GeV, was collected by the upgraded UA2 detector during the 1988 and 1989 runs of the CERN $\bar{p}p$ Collider at peak luminosities of up to 3×10^{30} $cm^{-2}s^{-1}$. This was used to calculate more precise values of the W and Z production cross sections times branching ratio $\sigma_W^e \equiv \sigma(\bar{p}p \rightarrow W + X) \cdot BR(W \rightarrow e\nu)$ and $\sigma_Z^e \equiv \sigma(\bar{p}p \rightarrow Z + X) \cdot BR(Z \rightarrow e^+e^-)$, giving a more significant comparison with theoretical predictions, including full QCD corrections to $O(\alpha_s)$ [3] and partial corrections to $O(\alpha_s^2)$ [4].

Many of the systematic uncertainties (both experimental and theoretical) which contribute to the individual cross sections σ_W^e and σ_Z^e are common. Hence it is of great interest to measure the cross section ratio [5]. This ratio can be expressed in terms of simpler quantities which can be evaluated in the context of the Standard Model (SM) :

$$R \equiv \frac{\sigma_W^e}{\sigma_Z^e} = \frac{\sigma_W}{\sigma_Z} \cdot \frac{\Gamma(W \rightarrow e\nu)}{\Gamma(W)} \cdot \frac{\Gamma(Z)}{\Gamma(Z \rightarrow e^+e^-)}$$

where $\sigma_W(\sigma_Z)$ is the total cross section for W (Z) production and the Γ's are the total and partial widths for boson decays. In this expression, the ratio of total cross sections and the partial widths depend on the basic gauge structure of the SM and are not sensitive to the particle content of the theory. The major uncertainty in these factors arises from the measurements of the parton distribution functions needed to compute the total cross sections. The total widths involve summing over all possible decay modes of the W and the Z, and are therefore sensitive to any non-standard decays of the bosons (regardless of whether or not they are observable).

In the past, this information has been used to place limits on the number of light neutrino generations [6]. Recent measurements by experiments at e^+e^- colliders [7,8], have now fixed the total Z width with relatively high precision, allowing R to be used to make a precise, albeit indirect, measurement of the total width of the W. This width is sensitive to the mass of the top quark (m_{top}) if $m_{top} + m_b < M_W$, where m_b is the mass of the b quark. It has the advantage that it is independent of the manner in which the top quark decays, whereas the direct top quark searches at hadron colliders assume that the value for the branching ratio BR(t $\rightarrow$ bev) is 1/9 as given by the SM. These direct searches by UA2 [9] and CDF [10] now exclude at the 95% Confidence Level a top quark with $m_{top} < 69$ GeV/c^2 and $m_{top} < 77$ GeV/c^2 respectively. More model independent analyses of SLC [11] and LEP data [12] suggest that $m_{top} > M_Z/2$ independent of the decay modes of the top quark. Thus if the observed value for R is significantly below that expected for a heavy top quark ($m_{top} > M_W$), this would

indicate a larger total W width, possibly arising from the W decaying into a top quark with suppressed semi-leptonic branching ratios.

In Section 2, a brief review of the upgraded UA2 detector is given. In Section 3, the electron and neutrino identification are explained. In Sections 4 and 5, the $W \rightarrow e\nu$ and $Z \rightarrow e^+e^-$ samples are discussed and the measured cross sections are given. In Section 6, the cross section values and the ratio R are compared with QCD predictions and a value of $\Gamma(W)$ is deduced. The significance of these results in the context of the SM is discussed.

2. UA2 APPARATUS

The UA2 detector was upgraded during the period 1985 to 1987. Details of the construction and performance of the various detector elements can be found in the references given below. Only the main features relevant to this analysis will be summarised here. They are :

i. increased calorimeter coverage to improve the measurement of the missing transverse momentum,
ii. a new central detector providing better electron identification,
iii. a three-level trigger system to handle the high event rates resulting from the high machine luminosity.

2.1 Calorimetry

A longitudinal view of a quadrant of the UA2 detector is shown in Fig. 1. The central calorimeter [13] was retained with minor modifications. It covers the full azimuthal range, $0° < \phi < 360°$ and polar angles $40° < \theta < 140°$. Each of the 240 electromagnetic and hadronic cells subtends 10° in θ and 15° in ϕ. The electromagnetic part is a multi-layer sandwich of lead and scintillator, 17 radiation lengths (r.l.) thick, while the hadronic part, consisting of two compartments, is an iron-scintillator sandwich, giving a thickness of 4.5 absorption lengths, including the electromagnetic compartment. In order to increase the radial space available for the new central detector, the thickness of the edge cell electromagnetic compartments was reduced. These edge cells cover the polar angles $40° < \theta < 50°$ and $130° < \theta < 140°$.

The forward calorimeters (end caps) [14] cover the pseudorapidity region $1 < |\eta| < 3$. Each end cap consists of 12 modules and each module is segmented into 16 cells. In a given module the two cells closest to the beam axis ($2.5 \leq |\eta| \leq 3.0$ and $2.2 \leq |\eta| \leq 2.5$) cover 30° in azimuth. The other cells have a constant segmentation of $\Delta\phi = 15°$, $\Delta\eta = 0.2$. All the cells in the pseudorapidity interval $1.0 \leq |\eta| \leq 2.5$ have one electromagnetic and one hadronic compartment. The electromagnetic compartment is a multi-layer sandwich of lead and scintillator, with a total thickness varying from 17.1 to

24.4 r.l. depending on the polar angle. The hadronic compartment is a multi-layer sandwich of iron and scintillator corresponding to ~ 6.5 absorption lengths, including the electromagnetic compartment. Each compartment is read out via two wavelength shifting plates placed on the opposite sides of each cell, introducing a dead space between adjacent cells of 7 mm for the electromagnetic compartments and of 13 mm for the hadronic ones. To minimise the effect of these dead spaces each module is rotated by 50 mrad around its symmetry axis normal to the beam.

Clusters of deposited energy were formed in the calorimeters by joining all cells with an energy greater than 400 MeV sharing a common edge. Clusters with a small lateral size and a leakage into the hadronic compartments consistent with a shower from a single isolated electron as measured from test beams were marked as electromagnetic. The condition that the cluster has a small lateral size was applied by calculating cluster sizes R_θ and R_ϕ. The cluster size R_θ (R_ϕ) is defined as the energy weighted r.m.s. deviations of the θ (ϕ) values of the cell centres for all cells in the cluster. The condition applied, R_θ, R_ϕ < 0.6 cell units, was fully efficient for isolated electrons. The requirement on the hadronic leakage was different in the three calorimeter regions because of the variation in the thickness of the electromagnetic compartments. The response of the calorimeter to hadronic showers depends on the energy fraction carried by photons. An average correction factor was defined for each compartment of the calorimeter and applied to the observed energies in hadronic showers in order to compensate for the difference in response. The factors applied to the electromagnetic cells were 1.18 in the central calorimeter and 1.20 in the end caps. In addition, a factor of 1.06 was applied to the second hadronic compartment in the central calorimeter to account for energy leaking through the back of the calorimeter.

2.2 Central Detector

The layout of the central detector is shown in Fig. 1. Around the beam-pipe, at radii of 3.5 cm and 14.5 cm, are two arrays of silicon counters (SI) used for tracking and ionisation measurements [15]. Between the two is a cylindrical drift chamber with jet geometry (the Jet Vertex Detector or JVD) [16]. After the inner tracking detectors is the Transition Radiation Detector (TRD) [17], consisting of two sets of radiators and proportional chambers. The outermost of the central detectors is the Scintillating Fibre Detector (SFD)[18] which consists of fibres arranged on cylinders into 6 stereo triplets followed by a 1.5 r.l. thick lead converter covering the central calorimeter, and a further 2 stereo triplets used to localise the early development of electromagnetic showers initiated in the lead converter ("preshower detector").

Charged tracks and the position of the event vertex along the beam axis were reconstructed using the SFD in conjunction with the silicon hodoscopes and the JVD. During high luminosity running there was a significant probability for the occurrence of more than one interaction in the same bunch crossing. Therefore the vertex finding

program searched for up to three vertices per event. The inefficiency for finding the highest multiplicity vertex, given that an electron track had been found, was negligible for vertices within 250 mm of the detector centre. Beyond 250 mm, the efficiency decreases mainly due to the limited acceptance of the inner silicon detector. Vertices beyond 250 mm were therefore rejected. The fraction of vertices inside this cut was measured to be $\varepsilon_V = 94.3 \pm 0.5\%$. The vertex finding inefficiency for events in which the W was not produced at the highest multiplicity vertex was not negligible, and an additional correction factor of 98.7% was applied to account for this effect.

The tracking and preshower sections of the SFD were used to match candidate electron tracks with the position of electromagnetic preshowers with a resolution of $\sigma_{r\phi} = 0.4$ mm in the r-ϕ plane (perpendicular to the beam axis) and $\sigma_z = 1.1$ mm along the beam direction. The quality of a track-preshower match was defined by the variable $d^2_\sigma = (\Delta_{r\phi}/\sigma_{r\phi})^2+(\Delta_z/\sigma_z)^2$ where $\Delta_{r\phi}$, Δ_z are the measured displacements between the track and preshower positions. The distribution of d^2_σ for a sample of central electrons from $W \rightarrow e\nu$ events is shown in Fig. 2(a). Accidental overlaps between photon showers and charged tracks give large values of d^2_σ, while electron candidates were required to have $d^2_\sigma < 25$ and a preshower cluster with a charge, detected in each of the three stereo views of the preshower detector, of at least twice that expected from a minimum ionising particle (MIP). A study of the background processes shows that for the sample shown in Fig. 2(a) the non-Gaussian tails beyond the cut of $d^2_\sigma < 25$ are not due to background but arise from a combination of shower fluctuations and systematic uncertainties in the track and preshower reconstruction.

2.3 Forward Detectors

In front of the forward calorimeters in the pseudorapidity range $1.1 < |\eta| < 1.6$ tracking and preshower information is provided by the End Cap Proportional Tubes (ECPT) [19], which consists of 16 modules ($\Delta\phi = 45^\circ$ each) of proportional tubes. In each module a stereo triplet behind a ~ 2 r.l. thick lead converter acts as a preshower detector, while two triplets in front of the converter act as tracking chambers. The resolution for the track-preshower match is 5 mm in each direction. The matching between tracks and preshower clusters for the ECPT is shown for a sample of $W \rightarrow e\nu$ events in Fig. 2(b). Candidate electrons were required to have a preshower cluster with $d^2_\sigma < 16$ and a charge greater than 20 MIP [19].

2.4 Trigger System

The trigger system consists of three levels, based on calorimeter information and signals from the Time of Flight counters (TOF, see Fig. 1) which were used to generate a minimum bias trigger signal. An outline of the trigger system is given below and more details can be found in Ref. [20].

i. The first level electron triggers used analogue sums of the signals from the photomultipliers of the electromagnetic calorimeter cells up to $|\eta| = 2$. The single electron trigger required a cluster of transverse energy deposition $E_T > 10$ GeV in any matrix of 2×2 adjacent cells in the electromagnetic calorimeter. The electron pair trigger required the simultaneous presence of two such clusters above a threshold of $E_T = 5$ GeV, separated in azimuth by at least 60°. At a luminosity of 2×10^{30} cm^{-2} s^{-1}, the rate of the single electron (electron pair) trigger was 15 (7) Hz.

ii. At the second level, electron and jet clusters were reconstructed in a fast processor using pedestal subtracted and gain corrected information from a fast digitisation of the calorimeter cell signals. Candidate electron clusters were required to have small lateral dimensions and small leakage into the hadronic calorimeter as expected for an isolated electron cluster. This reduced the rate of single electron (electron pair) triggers by a factor of 7 (12).

iii. At the third level, a pool of processors was used to perform the complete calorimeter reconstruction using the full calorimeter digitisation and a complete set of calibration constants. This enabled stricter cuts to be made on the cluster profiles for electron candidates and to reduce the rate for electron triggers to below 1 Hz at a luminosity of 2×10^{30} cm^{-2} s^{-1}. The third level processors were also used to make an approximate estimate of the transverse momentum balance of the event, $\not{p}_T$. In general, $W \rightarrow e\nu$ events have high p_T neutrinos which give rise to large values of $\not{p}_T$, while background processes tend to give small values of $\not{p}_T$. Therefore an estimate of $\not{p}_T$ was used in the selection of the $W \rightarrow e\nu$ sample. The value of $\not{p}_T$ was estimated online as the transverse component of the momentum balance

$$\vec{\not{p}}_T^{raw} = (-\Sigma E_{cell} \vec{u}_{cell})_T$$

where E_{cell} is the sum of the electromagnetic and hadronic compartment energies measured in each cell, corrected to account for the different response of these compartments to electromagnetic and hadronic showers, $\vec{u}_{cell}$ is a unit vector from the centre of the detector to the cell centre, and the sum extends over all calorimeter cells.

Two principal data samples were used in this analysis. The first sample (the "W sample") required an event to contain an electromagnetic cluster passing the third level cuts as well as a missing transverse momentum $\not{p}_T^{raw} > 15$ GeV/c. The cluster was required to have a transverse energy above 15 GeV, measured in the electromagnetic compartment only. The second sample (the "Z sample") consisted of events containing two electromagnetic clusters with $E_T > 5$ GeV both passing the third level electron cuts.

In addition the invariant mass of the pair of electromagnetic clusters was required to be above 25 GeV/c^2.

A third sample (the "inclusive electron sample") was based on data taken with a single electron trigger with a lower transverse energy threshold than for the W trigger. This sample was used to estimate the background contamination in the W sample.

In addition to the electron triggers discussed above, other triggers were employed which did not have the primary aim of selecting electrons. As a cross-check on the electron trigger and analysis, an independent estimate of σ_W^e was made using events from the missing transverse momentum trigger [21]. At the first level the $\not{p}_T$ trigger used a purpose-built fast electronics module to select events with large missing transverse momentum [22].This selection was refined at the second level and at the third level events were selected with $\not{p}_T^{raw} > 20$ GeV/c.

For 54% of the data taken the minimum bias trigger signal from the TOF counters was used in coincidence with the electron triggers described above. The efficiency of the TOF signal for $W \rightarrow e\nu$ events was measured from the data taken without the TOF coincidence to be $97.1 \pm 0.7\%$.

2.5 Luminosity

The luminosity was measured using eight scintillator telescopes at small angles to the beams, four on each side of the detector. These were formed by pairs of scintillation counters, 8 m and 10 m from the interaction point. Each pair of scintillation counters was read out in a tight timing coincidence, which was sensitive only to particles travelling outwards from the interaction region at the time of nominal beam crossing. The accumulated rates of these coincidences were used to compute the integrated luminosity using an algorithm which accounted for the effects of multiple interactions. The relative acceptance of this system compared to the TOF counters was measured from minimum bias data. The acceptance of the TOF counters was measured from data for which the detector readout was triggered by the beam crossing. The cross section seen by the system was computed by rescaling the measurement of the total cross section at $\sqrt{s} = 546$ GeV [23] to $\sqrt{s} = 630$ GeV, and subtracting elastic and single diffractive contributions.

The measured total luminosity accumulated by UA2 was 7.8 pb^{-1}. After removing data where not all of the detectors relevant to this analysis were functioning the useful luminosity was 7.4 ± 0.4 pb^{-1}, where the error is dominated by a 2.3% uncertainty on the acceptance of the luminosity telescopes and a 4.7% uncertainty on the total cross section.

The experimental value of the total cross section [23] depends on the ratio of the real to imaginary part of the forward scattering amplitude, ρ. The value of ρ measured by the UA4 experiment, $\rho = 0.24 \pm 0.04$, was used [24]. If instead one would use the value of ρ expected from dispersion theory, $\rho = 0.15$ [25], the luminosity would have to be decreased, and the cross sections reported in this paper increased by 3.6%.

3. ELECTRON AND NEUTRINO IDENTIFICATION

In this section the electron and neutrino identification are explained. Estimates of the electron efficiency and the resolution of the neutrino transverse momentum measurement are discussed.

3.1 Electron Identification and Efficiencies

The effects of the calorimeter electron selection applied in the second and third level trigger were studied for isolated electrons using electron test beam data. The energy leakage into the hadronic compartments was different for electrons hitting the shortened edge cells of the central calorimeter, the remaining cells of the central calorimeter and the end cap calorimeters. Therefore the efficiencies were measured separately for the three different regions and the results are shown in Table 1. The main loss of efficiency was for electrons impinging on the central calorimeter near an inter-cell boundary which tend to produce a larger leakage into the hadronic compartments. To exclude electrons with impact points near the edges of the central calorimeter where the showers would not be well contained, a fiducial volume cut was applied for the edge cells rejecting the electrons outside the region $42^\circ < \theta < 138^\circ$. In the forward regions, a fiducial volume cut was used to exclude a 30 mm wide region near the inter-cell boundary of constant azimuth where the electron selection efficiency was much lower.

Particles produced in association with the W (the "underlying event") can spoil the electron signature. This effect was studied by mixing data from test beam electrons with the underlying event from identified $W \rightarrow e\nu$ events. The resulting relative efficiencies to pass the electromagnetic cluster requirements are shown in Table 1. The effect is larger in the forward calorimeters because the energy flow per unit rapidity from the underlying event is larger than in the central region.

The lateral and longitudinal profiles of the shower were required to be consistent with those expected for a single isolated electron incident along the track direction as determined from extensive test beam data. From the observed and expected quantities and their estimated errors, a χ^2 test for the electron hypothesis was defined. Since most of the experimental distributions have significant non-Gaussian tails, $P(\chi^2)$ is not a true χ^2 probability but must be considered as a quality factor. Electron candidates with $P(\chi^2) < 10^{-4}$ were rejected. The surviving candidates were also required to have a preshower signal matching the track within the tolerances given in Sections 2.2 and

2.3. The efficiency of these cuts was measured from the data themselves; kinematic cuts were used to select a $W \rightarrow e\nu$ sample with negligible background and the efficiencies were measured by releasing the cuts one at a time. The results are given in Tables 1 and 2. The electron energy was corrected for the impact point dependence of the calorimeter response and the energy lost in the preshower detector as determined from test beam data.

3.2 Neutrino Identification

The neutrino transverse momentum was estimated offline by the transverse component of the momentum balance

$$\vec{p}_T^{\,\nu} \equiv \vec{\not{p}}_T = -\vec{p}_T^{\,e} - (\Sigma\, E_{cell}\, \vec{v}_{cell})_T$$

where $\vec{v}_{cell}$ is a unit vector from the interaction vertex to the cell centre and $\vec{p}_T^{\,e}$ is the electron transverse momentum corrected for the impact point. The sum extends over all cells in the calorimeter excluding the cells hit by the electron. The resolution on p_T^{ν} was studied using minimum bias and two-jet data in which high energy neutrino emission is not expected, allowing the observed value of the total missing transverse momentum to be used as a measure of the p_T^{ν} resolution. The distribution of $\not{p}_T$ for minimum bias data has the form [21]

$$\frac{dn}{d\not{p}_T^{\,2}} \propto \exp\left[-\frac{\not{p}_T^{\,2}}{\Delta^2}\right]$$

where the parameter Δ depends upon the total transverse energy in the event, E_T, and is well parameterised by $\Delta = \alpha(E_T)^{\beta}$ with $\alpha = 0.8$ and $\beta = 0.4$. No significant non-Gaussian tails are present above $\not{p}_T$ values of about 4 Δ which makes it straightforward to extract a very clean signal for $W \rightarrow e\nu$ (see Section 4).

4. W SAMPLE AND CROSS SECTION

The electron selection (Section 3.1) was used to determine a value for σ_W^e (Section 4.1). As a cross-check on this analysis, a value of σ_W^e was determined from a missing transverse momentum analysis (Section 4.2).

4.1 Electron Analysis

In order to determine suitable kinematic cuts to select a clean W sample, data from the 1988 inclusive electron sample corresponding to an integrated luminosity of 2.8 pb^{-1} were used. Only electron candidates with a transverse momentum $p_T^e > 20$ GeV/c were retained. The distribution of p_T^{ν} for this sample is shown in Fig. 3. A clear Jacobian peak from $W \rightarrow e\nu$ is visible at large p_T^{ν} whereas the region of low p_T^{ν} is dominated by fake electrons from QCD background. To estimate this background under

the W signal, its shape was measured using a sample of events with electromagnetic clusters. This sample was dominated by γ's from the decay of high p_T π°'s, and was used because γ's have a similar calorimeter response compared to electrons. The p_T^ν distribution of this sample was normalised to that of the electron sample for $p_T^\nu < 10$ GeV/c, where the electron sample is dominated by QCD background, and was used as a measure of that background (see Fig. 3). From this the fractional QCD background above $p_T^\nu > 20$ GeV/c was estimated to be ~ 1%. It was found that the residual background above $p_T^\nu > 20$ GeV/c tended to peak at low values of the transverse mass m_T defined as

$$m_T = \sqrt{2\, p_T^e\, p_T^\nu\, (1 - \cos\Delta\phi_{e\nu})}\,,$$

where $\Delta\phi_{e\nu}$ is the angle between $\vec{p}_T^{\,e}$ and $\vec{p}_T^{\,\nu}$. Therefore the final kinematic selection for the W sample was :

i. $p_T^e > 20$ GeV/c,

ii. $p_T^\nu > 20$ GeV/c,

iii. $m_T > 40$ GeV/c^2.

After this selection, the QCD background was found to be much less than 1% and was therefore neglected in the subsequent analysis. The W trigger stream was used to extract the $W \rightarrow e\nu$ signal corresponding to the full data sample. After applying the kinematic cuts (i)-(iii) above, the trigger thresholds used caused no additional loss of efficiency except in the central edge cells where the thickness of the electromagnetic compartment was reduced. For the central edge cells, the efficiency of the trigger thresholds on electrons from $W \rightarrow e\nu$ passing the kinematic selection (i)-(iii) above was measured to be 96.1 $\pm$ 1.8% using data taken with the inclusive electron trigger (Section 2.4). The distributions of p_T^e and p_T^ν are shown in Fig.4 for central electrons. Kinematic effects result in broader distributions for forward electrons as can be seen in Fig. 5.

The measured cross section is determined from the equation

$$\sigma_W = \frac{N_W - N_\tau}{\varepsilon\, \eta\, L}$$

where N_W is the observed number of W events, N_τ is the contribution from $W \rightarrow \tau\nu_\tau$ followed by the decay $\tau \rightarrow e\, \nu_e\, \nu_\tau$, η is the acceptance of the geometrical and kinematic selections, ε is the overall electron detection efficiency, and L is the integrated luminosity. The acceptance η was calculated using a Monte Carlo program which generated W or Z bosons according to the p_T and rapidity distributions of Ref. [3]. The Monte Carlo accounted for the effects of the event vertex distribution and for the

precise geometry of the tracking, preshower and calorimeter detectors. A parametrisation of the electron resolution as a function of track impact point based on test beam data was used. A simple model was used for the p_T^{ν} resolution, based on the transverse momentum balance in minimum bias, two-jet and $Z \rightarrow e^+e^-$ data. More details of the simulation are given in Ref. [26]. The Monte Carlo was also used to calculate the contribution from $W \rightarrow \tau \nu_\tau$ with the subsequent decay $\tau \rightarrow e \nu_e \nu_\tau$. The uncertainties on the acceptance were estimated by varying the structure functions, the p_T^W distribution and the calorimeter energy scale. The largest uncertainty was due to the structure functions because these affect the rapidity distribution of the W. The differences between the structure functions produce a larger variation in the forward regions than in the central region. The resulting cross sections for the three calorimeter regions are given in Table 3.

Since the results for the three calorimeter regions are in good agreement, they can be combined to give a best estimate of the W cross section using weights proportional to the product of efficiency and acceptance for each region; the errors were calculated using the procedure explained in Section 6 :

$$\sigma_W^e = 660 \pm 15(\text{stat}) \pm 37(\text{syst}) \text{ pb.}$$

This procedure is also used to evaluate σ_Z^e and is more reliable for combining results from small event samples than the use of weights proportional to the number of observed events. The result is slightly larger than the values published previously [1,2], but is consistent within the statistical and systematic errors.

4.2 W Sample from the Missing p_T Analysis

As a cross-check on the electron analysis, an independent estimate of σ_W^e for the central non-edge region was obtained using the missing transverse momentum signature of $W \rightarrow e\nu$ decays, without using the electron identification criteria described above. Events were selected from the $\not{p}_T$ sample (see Section 2.4). The $W \rightarrow e\nu$ signal was statistically separated from the background processes by the study of cluster shape variables probing the lateral and longitudinal development of showers in the non-edge cells of the central calorimeter. No information from the tracking or preshower detectors was used and therefore there were significant backgrounds from QCD two-jet events and from beam halo particles hitting the calorimeter. QCD jets give rise to larger clusters with more leakage into the hadronic compartments than electrons. Clusters arising from beam halo tend to be elongated along the beam direction. Therefore the following three variables were defined to separate the signal from these two background sources :

i. the electromagnetic energy fraction in the cluster $f_{EM} = E_{EM}/E$, where E_{EM} (E) is the electromagnetic (total) cluster energy,

ii. the lateral cluster profile $P_r = (E_1 + E_2)/E$, where E_1 and E_2 are the two highest cell energies in the cluster,
iii. the cluster radius asymmetry $A_R = (R_\theta - R_\phi)/(R_\theta + R_\phi)$, where R_θ and R_ϕ are the cluster radii along the θ and ϕ directions as defined in Section 2.1.

The variables f_{EM} and P_r provide good discrimination between the electron signal and the QCD background, whereas A_R discriminates between signal and beam halo background. For each of the three variables the $\not{p}_T$ sample was fitted to a combination of signal, QCD background, and beam halo background, and hence three estimates of the electron signal were evaluated. The three fits produced compatible results, giving confidence in the procedure. The systematic error in the fit procedure accounts for the differences in the fit results for the three variables used and for uncertainties in the signal and background probability distribution functions used. The contribution from $W \rightarrow \tau\, \nu_\tau$ with the subsequent decay $\tau \rightarrow e\, \nu_e\, \nu_\tau$ is estimated to be 2% in this analysis, and is neglected. The result

$$\sigma_W^e = 656 \pm 27(\text{stat}) \,^{+66}_{-80}(\text{syst})\ \text{pb}$$

agrees well with the one quoted above from the electron analysis. The systematic error is dominated by the uncertainties in the calorimeter cluster shape variable analysis and the luminosity. The uncertainty on the luminosity is correlated with the error on the value of σ_W^e from the electron analysis (Section 4.1).

A more powerful comparison can be made by performing the calorimeter cluster shape analysis on an event sample with the $W \rightarrow e\nu$ events identified by the electron analysis removed. The signal found in this way was used to measure the inefficiency of the electron selection. The errors on the acceptances and efficiencies related to the cluster shape variable analysis approximately cancel, and the result for the overall efficiency to identify an electron in a $W \rightarrow e\nu$ event was found to be $63 \pm 1(\text{stat}) \,^{+1}_{-2}(\text{syst})$ %, in good agreement with the value obtained in the electron analysis $64 \pm 1(\text{stat}) \pm 1(\text{syst})$ %.

5. Z SELECTION

The sample of events containing at least two electromagnetic clusters satisfying the third level Z-trigger requirements (Section 2.4) with invariant mass m_{ee} greater than 40 GeV/c^2 has been used to evaluate the cross section σ_Z^e for the process $Z \rightarrow e^+e^-(\gamma)$. When there was a third electromagnetic cluster in the event with a transverse energy greater than 5 GeV, it was included in the invariant mass calculation, thereby retaining candidates for the decay $Z \rightarrow e^+e^-\gamma$. The m_{ee} distribution (Fig. 6) shows a clear peak at the Z mass while at lower mass values it is dominated by two-jet events from QCD production, with a small contribution of Drell-Yan pairs. Two different fits were made to the mass spectrum for use in the calculation of the QCD background under the Z

peak. The first fit used a superposition of a Gaussian resonance and a background with the form A m_{ee}^{-B} and the fit range was $40 < m_{ee} < 160$ GeV/c^2 (solid line in Fig. 6). The second fit used the range $40 < m_{ee} < 70$ GeV/c^2 and contained only the background term (dashed line in Fig. 6).

The requirement that at least one cluster satisfies the electron selection criteria described in Section 3.1 reduces the sample to the one shown in Fig. 7. The rejection factors of the electron cuts in the central, edge and forward regions were calculated from the reduction of events in the background mass region. Since the background levels and the selection efficiencies are different in the three calorimeter regions, the six sub-samples of electron pair candidates resulting from the combinations of the three different regions have been treated separately throughout the analysis.

The QCD background under the Z peak was estimated by extrapolating the fitted background distribution of Fig. 6 under the Z peak and applying the rejection factors calculated for the electron selection criteria. For the sample shown in Fig. 7, it is in the range 5% to 20%, depending on the sub-sample, too high to allow an accurate measurement of the signal. On the other hand, the requirement that both clusters satisfy the standard electron selection, while reducing the background to less than 0.5%, has an efficiency which is of the order of 50%. However, a more efficient selection is possible because of the increased rejection of the electron pair signature. Since the majority of electrons from Z decays are in the central region, where the rejection of the UA2 detector is observed to be higher than in the forward regions, looser requirements have been studied for central electrons in order to increase the selection efficiency. As shown in Table 2, a large fraction of the inefficiency results from the tracking and preshower requirements. In order to recover events lost because of the track inefficiency, electron candidates were required to have at least 10 hit fibre layers (out of a total of 18) in a ±2.5 mm window in front of a preshower cluster. Similarly, electron candidates rejected because of the internal matching requirements for preshower clusters [18] or failing the tight track-preshower matching were recovered by selecting tracks accompanied by a charge greater than twice that expected from a minimum ionising particle in the 6 fibre layers of the preshower detector in a ±2.5 mm window around the extrapolated track position in the preshower layers. The requirement that a central electron pass either the standard or the looser track-preshower matching has an efficiency of 97.1 ± 0.5(stat) ± 0.6(syst) %, as measured from a background-free W sample. The rejection against the QCD background is reduced by a factor of three, relative to the standard electron selection. The QCD background was estimated using the two fits discussed above. The average value of the two fits was used and the difference was used as an estimate of the systematic error.

The final Z sample was obtained by requiring events in which at least one cluster satisfied the standard electron cuts and a second cluster which satisfied either the standard or the looser selection criteria. The final sample contains seven events with

three electromagnetic clusters of which none has the third cluster satisfying the electron criteria. These events are all compatible with the radiative decay hypothesis. The comparison of these events with the SM expectations is outside the scope of the present paper. The invariant mass distribution of the final Z sample is shown in Fig. 8.

The number of events and the QCD background in the region $76 < m_{ee} < 110$ GeV/c^2 are summarized in Table 4 for the six sub-samples, together with the acceptances as determined from the same Monte Carlo program used for the $W \rightarrow e\nu$ process. The contribution from single photon exchange and γ^*Z interference terms in the same mass region is 1.65 %. The values of σ_Z^e for each sub-sample, also shown in Table 4, are determined from

$$\sigma_Z^e = (N_Z - N_{QCD}) \cdot \frac{(1-f_{\gamma^*})}{\varepsilon \eta L}$$

where N_Z is the number of Z candidates, N_{QCD} is the number of QCD background events, f_{γ^*} is the relative contribution from single photon exchange and γ^*Z interference terms, ε is the efficiency, η is the acceptance, and L is the integrated luminosity. The results for the six regions are in good agreement and were combined with the same procedure used for σ_W^e (Section 4) to give

$$\sigma_Z^e = 70.4 \pm 5.5(\text{stat}) \pm 4.0(\text{syst}) \text{ pb.}$$

If the mass window is increased to $70 < m_{ee} < 160$ GeV/c^2, the value of σ_Z changes by less than 0.5%. The result is in good agreement with the previous measurements [1,2]. There are 54 events in the mass interval 40-70 GeV/c^2, which is in good agreement with the expected 24 ± 2 Drell-Yan events plus 32 ± 5 QCD background events. As indicated in Fig. 8, one event with $m_{ee} = 278$ GeV/c^2 is in the final Z sample. The expected number of Drell-Yan pairs with masses greater than 160 GeV/c^2 is 0.3 events.

6. COMPARISONS WITH SM PREDICTIONS

The measured values for σ_W^e and σ_Z^e can be compared with the SM predictions. In order to perform these comparisons, the following ingredients have been used :

i. calculations of the partial widths for all W and Z decays expected to occur in the SM. When there are quarks in the final state, $O(\alpha_S)$ QCD corrections have been applied, including the effect of non-zero masses for the t and b quarks [27],

ii. the total W and Z cross sections calculated at three different perturbative orders :

- Born level,
- including the $O(\alpha_S)$ QCD corrections [3],
- including a partial calculation of the $O(\alpha_S^2)$ corrections [4].

The theoretical predictions depend on a small number of basic parameters. The value for α_S was computed using Λ_{QCD} from the parton distribution functions and a scale $Q^2 = M_W^2$ (M_Z^2) for the case of the W(Z). The Z mass, computed from a weighted average of LEP [8] and SLC [7] results, was taken to be 91.15 GeV/c^2. The recent UA2 value of M_W/M_Z [28] was used to compute the weak mixing angle $\sin^2\theta_W$ = 0.220 and to derive the W mass, M_W = 80.5 GeV/c^2. A serious uncertainty arises from the parton distribution functions [29]. Several recent sets were chosen to provide a plausible estimate of the uncertainty. The standard set was DFLM with Λ_{QCD} = 160 MeV [30], which has been evaluated using next-to-leading order QCD calculations and the DIS regularisation scheme. Two alternative sets MRSE' and MRSB'[31] obtained from next-to-leading order QCD calculations performed in the $\overline{MS}$ scheme were also used. The cross section calculation correctly accounts for the regularisation scheme dependence. The comparison of the SM prediction for σ_W^e with the data is shown in Fig. 9. The dependence of the prediction on m_{top} arises from the change in the total width of the W as the $W \rightarrow t\bar{b}$ decay channel becomes kinematically suppressed. It is apparent that the parton distribution function uncertainties are large but there are additional uncertainties due to the QCD corrections. The $O(\alpha_S)$ correction to the total cross section amounts to an increase of 30% and partial calculations of the $O(\alpha_S^2)$ corrections [4] indicate an additional increase in the cross section by 10%. The measurements are inconsistent with the pure Born level cross sections but are not sufficiently precise to distinguish between the $O(\alpha_S)$ and the $O(\alpha_S^2)$ QCD corrections. Despite these ambiguities, the measurement agrees with the SM expectation with a heavy top quark and agrees rather poorly with the expectation for a light top quark. However, no quantitative conclusion on the mass of the top quark can be made because of these ambiguities, including the uncertainty on the incomplete $O(\alpha_S^2)$ QCD corrections.

A similar comparison for σ_Z^e is made in Fig. 10. The measured value of σ_Z^e is in good agreement with the SM prediction.

The results for σ_W^e and σ_Z^e were used to calculate a value for the cross section ratio R. In order to propagate the errors correctly, a simple Monte Carlo technique was used. The procedure generated Monte Carlo "experiments" using Poisson statistics for the observed number of events. The parts of the systematic error that were of a statistical nature were generated from Gaussian distributions and the remaining parts were generated from a uniform box distribution. The procedure correctly took into account the parts of the systematic error such as the luminosity that are fully correlated between σ_W^e and σ_Z^e and the parts that are partially correlated such as the electron efficiencies. The result is

$$R = 9.38\ ^{+0.82}_{-0.72}(\text{stat}) \pm 0.25\ (\text{syst}).$$

After combining the statistical and systematic errors the 90% confidence interval for R is

$$8.2 < R < 10.9\ .$$

The result is compared to the SM predictions in Fig. 11. Most of the theoretical uncertainties, including the effect of the higher order QCD corrections, are expected to almost completely cancel [4,32] in this ratio. The uncertainties on the absolute values of the structure functions cancel and the residual uncertainty is due to the lack of knowledge of the ratio of the valence structure functions $u_V(x)/d_V(x)$. The parametrisations [31] take into account a reasonable variation of this ratio by considering all the available data, including the preliminary measurement of $u_V(x)/d_V(x)$ by the NMC collaboration [33]. From Fig. 11 the measured value of R is compatible with the heavy top quark hypothesis but the experimental error on R is too large to exclude a light top quark.

Finally, within the context of the SM, it is possible to use the observed value for R to extract a value for the total W width. Using the values for M_W and M_Z quoted above, the ratio of the widths can be determined from the equation

$$\frac{\Gamma(W)}{\Gamma(Z)} = \frac{\sigma_W}{\sigma_Z} \cdot \frac{\Gamma(W \to e\nu)}{\Gamma(Z \to e^+e^-)} \cdot \frac{1}{R}$$

where the first two factors of the right hand side do not depend on the value assumed for the top quark mass. The uncertainties on the first two factors have been investigated by varying the parton distribution functions and changing the value of $\sin^2\theta_W$ from the value determined by UA2 [28] to the world average value determined from low energy neutrino experiments [34] while keeping M_Z fixed. The results are shown in Table 5 below. After computing the 68% confidence interval for the measured value of 1/R, and using the first value given in Table 5, the ratio of the widths is

$$\Gamma(W)/\Gamma(Z) = 0.902 \pm 0.074(\text{stat}) \pm 0.024(\text{syst})$$

where the systematic error reflects the experimental uncertainties only. A value for $\Gamma(W)$ can be deduced using the weighted average of SLC [7] and LEP [8] results for the Z width, $\Gamma(Z) = 2.546 \pm 0.032$ GeV. This leads to

$$\Gamma(W) = 2.30 \pm 0.19(\text{stat}) \pm 0.06(\text{syst})\ \text{GeV}$$

where the errors reflect the experimental errors only. If the theoretical uncertainties are reflected in the variations given in Table 5, they correspond to < 50 MeV/c^2 uncertainty

on $\Gamma(W)$. This value is in good agreement with a recent determination using an equivalent method by the CDF collaboration [35]. In the SM the width of the W is expected to decrease from 2.8 Gev to 2.1 GeV as m_{top} is increased from zero to M_W. The measured value is in agreement with the SM expectation in the case of a heavy top quark, and is inconsistent with a light top quark. At the 90% (95%) Confidence Level $\Gamma(W) < 2.56$ GeV/c^2 (2.64 GeV/c^2).

7. CONCLUSIONS

Results for the W and Z production cross sections times branching ratio to electrons have been presented from large samples of $W \rightarrow e\nu$ and $Z \rightarrow e^+e^-$ events accumulated by the upgraded UA2 detector. The measured value of σ_W^e is in good agreement with the Standard Model (SM) expectations for the case of a heavy top quark but in poor agreement with the case of a light top quark. The measured value of σ_Z^e is also in good agreement with the SM expectations. The measured value of the cross section ratio R agrees with the SM prediction using three generations of light neutrino species. The value of R was used to determine the total width of the W to be $\Gamma(W) = 2.30 \pm 0.19(stat) \pm 0.06(syst)$ GeV.

ACKNOWLEDGEMENTS

We gratefully acknowledge P. Darriulat for his contributions and guidance during the design and construction of the UA2 upgrade project.

The technical staff of the institutes collaborating in UA2 have contributed substantially to the construction and operation of the experiment. We deeply thank them for their continuous support. The experiment would not have been possible without the very successful operation of the improved CERN $\bar{p}p$ Collider whose staff and coordinators we sincerely thank for their collective effort. We thank T. Matsuura and W.J. Stirling for helpful discussions and for letting us use their calculations of the W and Z cross sections in the form of computer programs.

Financial support from the Schweizerischen Nationalfonds zur Förderung der Wissenschaftlichen Forschung to the Bern group, from the UK Science and Engineering Research Council to the Cambridge group, from the Bundesministerium für Forschung und Technologie to the Heidelberg group, from the Institut National de Physique Nucléaire et de Physique des Particules to the Orsay group, from the Istituto Nazionale di Fisica Nucleare to the Milano, Pavia, Perugia and Pisa groups and from the Institut de Recherche Fondamentale (CEA) to the Saclay group are acknowledged.

Table 1

Efficiencies of the calorimeter electron selection (%) for the three calorimeter regions.

	Central Non-Edge	Central Edge Cells	Forward
Efficiency for isolated electrons	92.6 ± 0.9	93.5 ± 2.5	99.2 ± 0.8
Effect of W underlying event	99.0 ± 0.5	98.3 ± 0.5	96.3 ± 0.8
Electron Quality $P(\chi^2 > 10^{-4})$	95.1 ± 1.2	94.2 ± 3.4	93.9 ± 2.2
Overall Calorimeter Efficiency	87.2 ± 1.5	86.6 ± 3.9	89.7 ± 2.3

Table 2

Track and preshower efficiencies (%) for the two tracking regions.
The first error is statistical and the second error is systematic.

	Central	Forward
Track Efficiency	90.6 ± 0.8 ± 0.8	96.1 ± 1.2 ± 3.3
Combined Track-Preshower Efficiency	79.6 ± 0.9 ± 1.0	91.4 ± 1.9 ± 1.3

Table 3

Calculation of σ_W^e for the three calorimeter regions. The first error on σ_W^e is statistical and the second error is systematic.

	Acceptance (%)	τ background Events	Number of Events	σ_W^e (pb)
Central Non-Edge	44.5 ± 1.7	53.4 ± 1.4	1406	645 ± 18 ± 38
Central Edge cells	8.5 ± 0.4	10.3 ± 0.3	270	676 ± 43 ± 48
Forward	8.9 ± 0.8	12.0 ± 1.1	365	710 ± 39 ± 55
Combined			2041	660 ± 15 ± 37

Table 4

Calculation of σ_Z^e. The abbreviations Ce (central calorimeter non-edge cells), Ed (central calorimeter edge cells), and Fd (forward calorimeter) are used. The first error on σ_Z^e is statistical and the second error is systematic.

	Acceptance (%)	QCD Background Events	Number of Events	σ_Z^e (pb)
Ce-Ce	20.6 ± 0.5	0.32 ± 0.08	65	65.6 ± 8.5 ± 4.0
Ce-Ed	9.4 ± 0.4	0.66 ± 0.14	36	79.3 ± 13.4 ± 5.2
Ce-Fd	13.8 ± 0.5	0.44 ± 0.12	48	72.0 ± 10.6 ± 4.6
Ed-Ed	1.1 ± 0.2	0.26 ± 0.16	3	52.2 ± 32.8 ± 7.9
Ed-Fd	2.9 ± 0.2	0.50 ± 0.14	11	76.8 ± 23.9 ± 5.8
Fd-Fd	1.8 ± 0.5	0.21 ± 0.07	6	67.8 ± 27.7 ± 12.1
Combined		2.39 ± 0.30	169	70.4 ± 5.5 ± 4.0

Table 5

Dependence of the measured ratio of widths $\Gamma(W)/\Gamma(Z)$ on the input assumptions. The parton distributions and weak mixing angle have been varied, as discussed in the text.

Parton distributions	$\sin^2\theta_W$ value	source	$\frac{\sigma_W}{\sigma_Z}$	$\frac{\Gamma(W \to e\nu)}{\Gamma(Z \to e^+e^-)}$	$\frac{\Gamma(W)}{\Gamma(Z)}$
DFLM	0.220	UA2 [26]	3.116	2.717	0.902
MRSB'	0.220	UA2 [26]	3.080	2.717	0.892
MRSE'	0.220	UA2 [26]	3.172	2.717	0.919
DFLM	0.231	DIS [33]	3.207	2.683	0.917

REFERENCES

[1] UA1 Collaboration, C. Albajar et al., Z. Phys. C44 (1989) 15.

[2] UA2 Collaboration, R. Ansari et al., Phys. Lett. B194 (1987) 158.

[3] G. Altarelli et al., Z. Phys. C27 (1985) 617;
W.J. Stirling, private communication.

[4] T. Matsuura, 'Higher Order Corrections to the Drell-Yan Process', Ph. D. Thesis, University of Leiden, 1989;
T. Matsuura and W.L. van Neerven, Z. Phys. C38 (1988) 623;
T. Matsuura, S.C. van der Marck, and W.L. van Neerven, Phys. Lett. B211 (1988) 171 and Nucl. Phys. B319 (1989) 570.

[5] N. Cabibbo, Proceedings of the Third Topical Workshop on Proton-Antiproton Collider Physics, CERN 83-04 (1983) 567;
F. Halzen and K. Mursula, Phys. Rev. Lett. 51 (1983) 857;
Ken-ichi Hikasa, Phys. Rev. D29 (1984) 1939;
A.D. Martin, R.G. Roberts, and W.J. Stirling, Phys. Lett. B189 (1987) 220;
F. Halzen, C.S. Kim, and S. Willenbrock, Phys. Rev. D37 (1988) 229.

[6] UA2 Collaboration, R. Ansari et al., Phys. Lett. B186 (1987) 440;
UA1 Collaboration, C. Albajar et al., Phys. Lett. B198 (1987) 271;
P. Colas, D. Denegri, and C. Stubenrauch, Z. Phys. C40 (1988) 527.

[7] MARK II Collaboration, G. Abrams et al., Phys. Rev. Lett. 63 (1989) 2173.

[8] ALEPH Collaboration, D. Decamp et al., Phys. Lett. B231 (1989) 519 and CERN-EP/89-168;
DELPHI Collaboration, P. Aarnio et al., Phys. Lett. B231 (1989) 539;
L3 Collaboration, B. Adeva et al., Phys. Lett. B231 (1989) 509 and L3 Preprint #004;
OPAL Collaboration, M.Z. Akrawy et al., Phys. Lett. B231 (1989) 530.

[9] UA2 Collaboration, T. Åkesson et al., CERN-EP/89-152, submitted to Z. Phys. C.

[10] CDF Collaboration, F. Abe et al., Phys. Rev. Lett. 64 (1990) 142.

[11] MARK II Collaboration, G.S. Abrams et al., Phys. Rev. Lett. 63 (1989) 2447.

[12] OPAL Collaboration, M.Z. Akrawy et al., CERN-EP/89-154, submitted to Phys. Lett. B;
ALEPH Collaboration, D. Decamp et al., CERN-EP/89-165, submitted to Phys. Lett. B.

[13] A. Beer et al., Nucl. Instr. Meth. A224 (1984) 360.

[14] F. Alberio et al., The Electron, Jet and Missing Transverse Energy Calorimetry of the Upgraded UA2 Experiment at the CERN $\bar{p}p$ Collider, in preparation for Nucl. Instr. Meth.

[15] R. Ansari et al., Nucl. Instr. Meth. A279 (1989) 388.

[16] F. Bosi et al., Nucl. Instr. Meth. A283 (1989) 532.

[17] R. Ansari et al., Nucl. Instr. Meth. A263 (1988) 51.

[18] R.E. Ansorge et al., Nucl. Instr. Meth. A265 (1988) 33;
J. Alitti et al., Nucl. Instr. Meth. A279 (1989) 364.
[19] K.Borer et al., Nucl. Instr. Meth. A286 (1990) 128.
[20] G. Blaylock et al., The Multi-Level Trigger and Data Acquisition System of the Upgraded UA2 Experiment at the CERN $\bar{p}p$ Collider, in preparation for Nucl. Instr. Meth.
[21] UA2 Collaboration,J. Alitti et al., CERN-EP/89-151, submitted to Phys. Lett. B.
[22] P. Moreira and G. Polesello, CERN-EP/89-110, to be published in Nucl. Instr. Meth.
[23] UA4 Collaboration, M. Bozzo et al., Phys. Lett. B147 (1984) 392.
[24] UA4 Collaboration, D.Bernard et al., Phys. Lett. B198 (1987) 583.
[25] U. Amaldi et al., Phys. Lett. B66 (1977) 390;
A. Martin, Proceedings of the Workshop on $\bar{p}p$ Collider Physics (Bern 1984) 308.
[26] UA2 Collaboration, J. Alitti et al., Measurement of the Transverse Momentum Distributions of W and Z Bosons at the CERN $\bar{p}p$ Collider, in preparation.
[27] T. Alvarez, A. Ceites, and J. Terron, Nucl. Phys. B301 (1988) 1;
D. Albert, W.J. Marciano, D. Wyler, and Z. Parsa, Nucl. Phys. B166 (1980) 460.
[28] UA2 Collaboration, J. Alitti et al., A Precise Determination of the W and Z Masses at the CERN $\bar{p}p$ Collider, in preparation.
[29] A.D. Martin, R.G. Roberts, and W.J. Stirling, Phys. Lett. B207 (1988) 205.
[30] M. Diemoz, F. Ferroni, E. Longo, and G. Martinelli, Z. Phys. C39 (1988) 21.
[31] A.D. Martin, R.G. Roberts, and W.J. Stirling, Phys. Lett. B206 (1988) 327 and Mod. Phys. Lett. A4 (1989) 1135.
[32] D.A. Dicus and S. Willenbrock, Phys. Rev. D34 (1986) 148.
[33] NMC Collaboration: M.A.J. Botje, Proceedings of the 19th Symposium on Multiparticle Dynamics, Arles (1988), eds. D. Schiff and J. Tran Than Van, Editions Frontières, page 237;
NMC Collaboration: presented by J. Nassalski at the International EPS Conference on High Energy Physics, Madrid, September 1989.
[34] G.L. Fogli and D. Haidt, Z. Phys. C40 (1988) 379.
[35] CDF Collaboration, F. Abe et al., Phys. Rev. Lett. 64 (1990) 152.

FIGURE CAPTIONS

Fig. 1 Schematic longitudinal view of the UA2 detector showing one quadrant.

Fig. 2 Distribution of the normalised track-preshower match d^2_σ for electron candidates (a) in the central detector, and (b) in the forward detectors.

Fig. 3 Distribution of p_T^ν from the partial inclusive electron trigger sample. The dashed curve is the estimated QCD background (see text).

Fig. 4 Transverse momentum distributions for events with electrons in the central calorimeter (edge and non-edge cells combined).

Fig. 5 Transverse momentum distributions for events with electrons in the forward calorimeters.

Fig. 6 The invariant mass spectrum for electron pair candidates satisfying the calorimeter electron selection criteria. The curves show the result of the fits explained in the text.

Fig. 7 The invariant mass spectrum for electron pair candidates satisfying the calorimeter electron selection criteria and at least one cluster satisfying the full electron selection criteria.

Fig. 8 The invariant mass spectrum for the sample with two clusters satisfying the full electron identification criteria. One event has $m_{ee} = 278$ GeV/c^2.

Fig. 9 Comparison of the measured σ_W^e with Standard Model predictions as a function of m_{top}. The shaded band represents the 1σ confidence interval, combining statistical and systematic errors in quadrature. The three solid curves indicate the results of the cross section calculations described in Section 6, using the DFLM parton distribution functions. The upper dashed curve uses the MRSB' parametrisations, while the lower dashed curve uses the MRSE' parametrisations.

Fig. 10 Comparison of the measured σ_Z^e with Standard Model predictions as a function of m_{top}. The curves have the same meaning as those shown in Fig. 9.

Fig. 11 Comparison of the measured ratio R with Standard Model predictions as a function of m_{top}. The shaded band represents the 1σ confidence interval; the hashed region is excluded at 90% confidence level. The lower solid curve corresponds to the predicted value using the DFLM parton distribution functions and assuming three light neutrinos. The thickness of this line represents the variation observed between the Born, $O(\alpha_S)$, and $O(\alpha_S^2)$ calculations. The upper dashed curve uses the MRSE' parametrisations while the lower dashed curve uses the MRSB' parametrisations. The upper solid curve corresponds to four light neutrinos using the DFLM parametrisations.

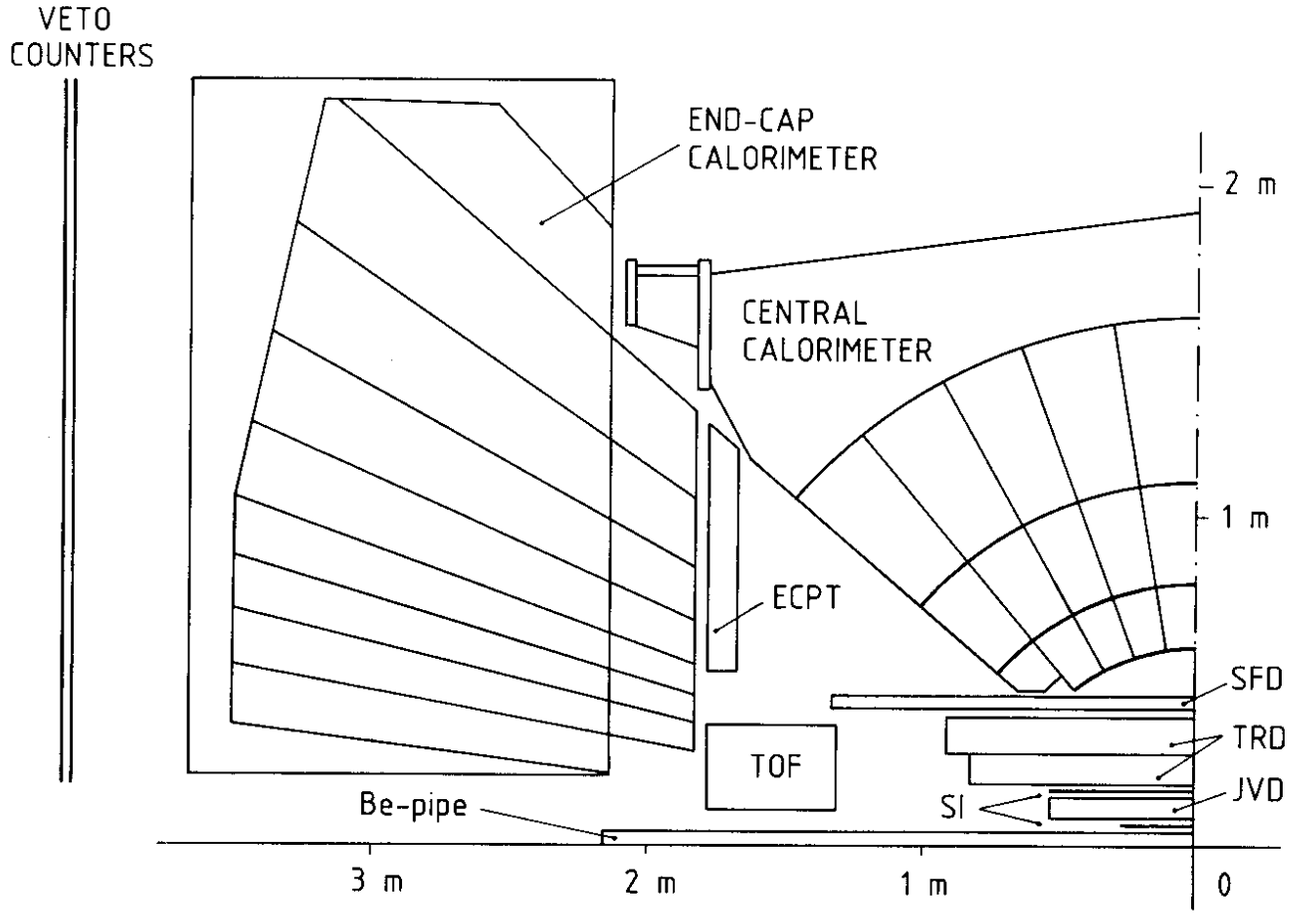
VETO
COUNTERS
END-CAP
CALORIMETER
2 m
CENTRAL
CALORIMETER
1 m
ECPT
SFD
TRD
TOF
JVD
SI
Be-pipe
3 m
2 m
1 m
0

Fig. 1

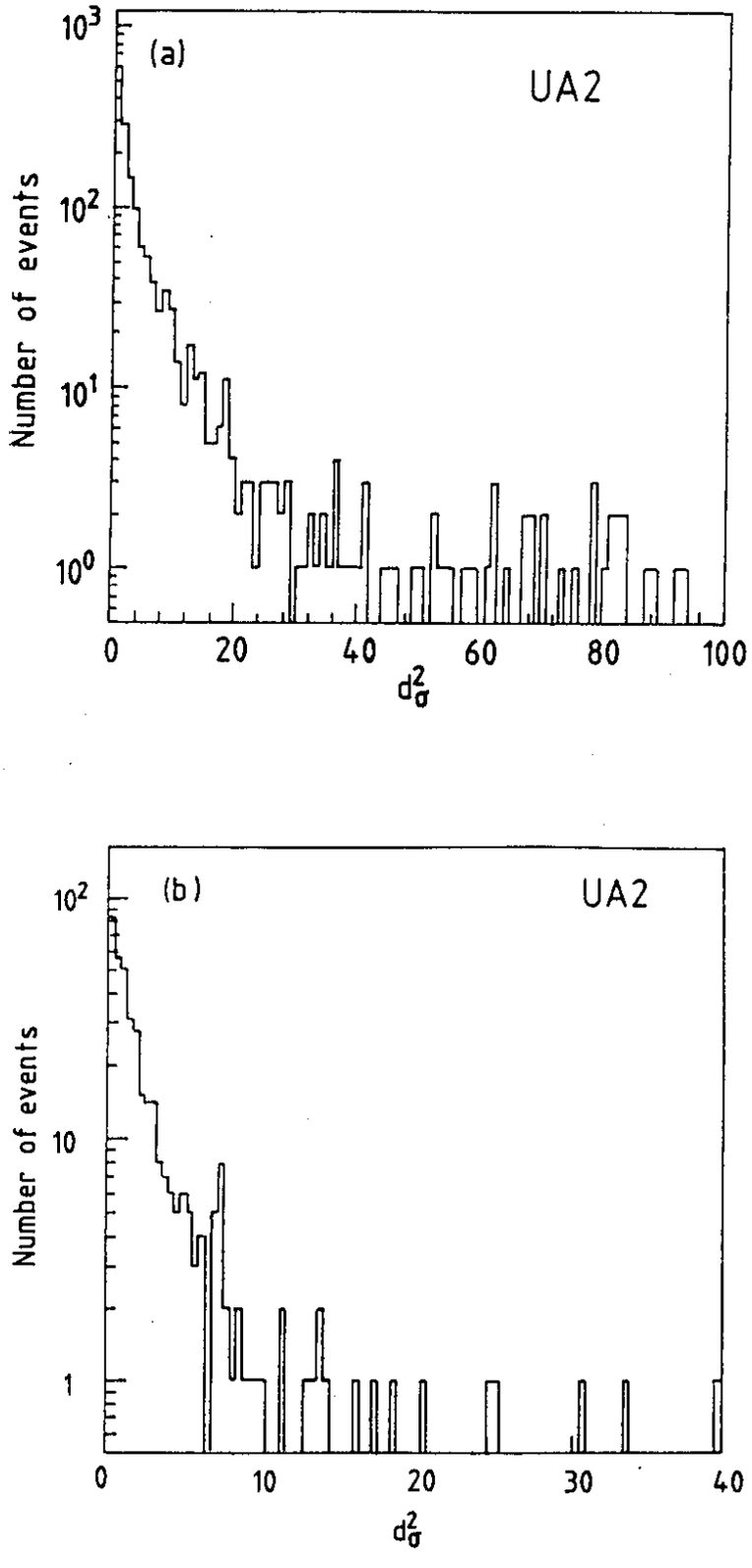
(a)
UA2
Number of events
10^3
10^2
10^1
10^0
0
20
40
60
80
100
d^2_σ
(b)
UA2
Number of events
10^2
10
1
0
10
20
30
40
d^2_σ

Fig. 2

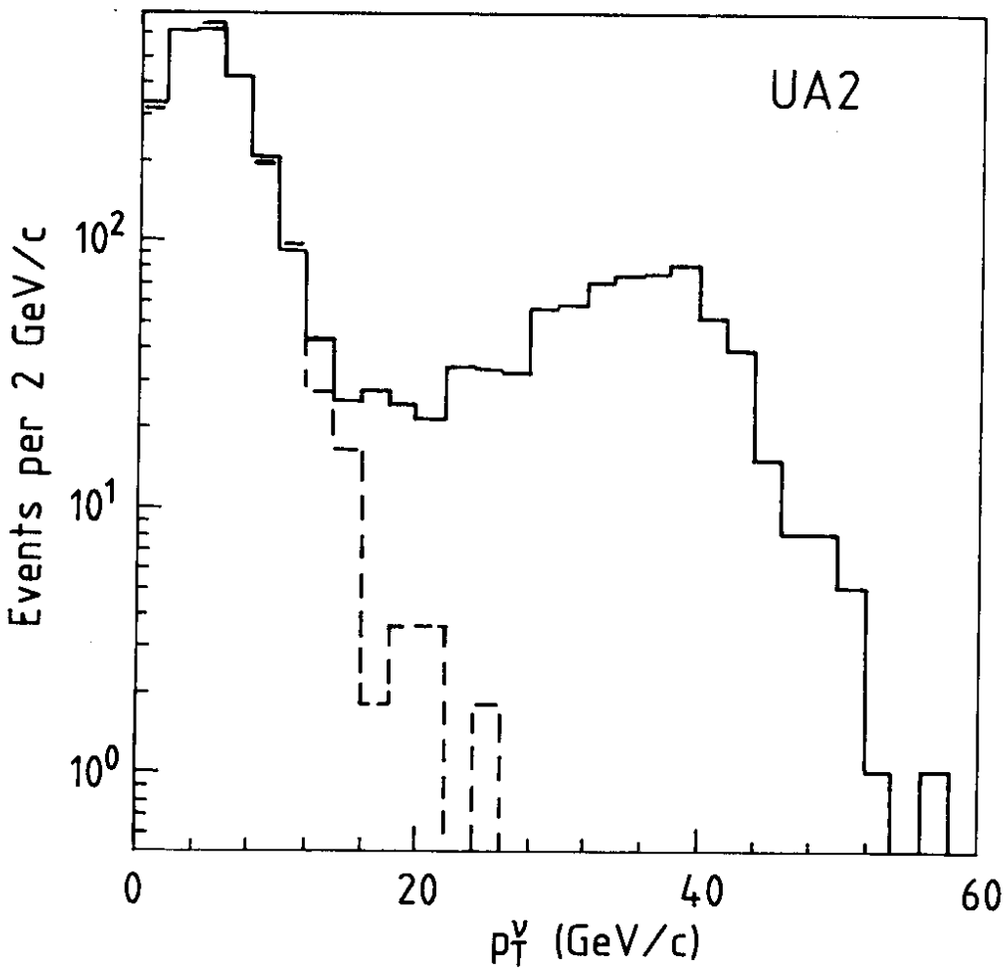

Fig. 3

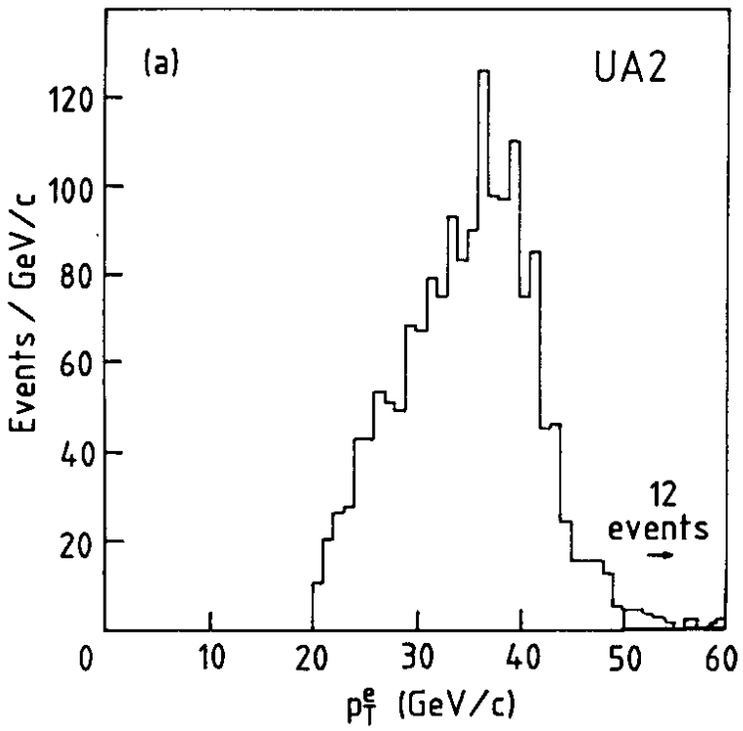
(a)
UA2
Events / GeV/c
120
100
80
60
40
20
0
10
20
30
40
50
60
12
events
p_T^e (GeV/c)

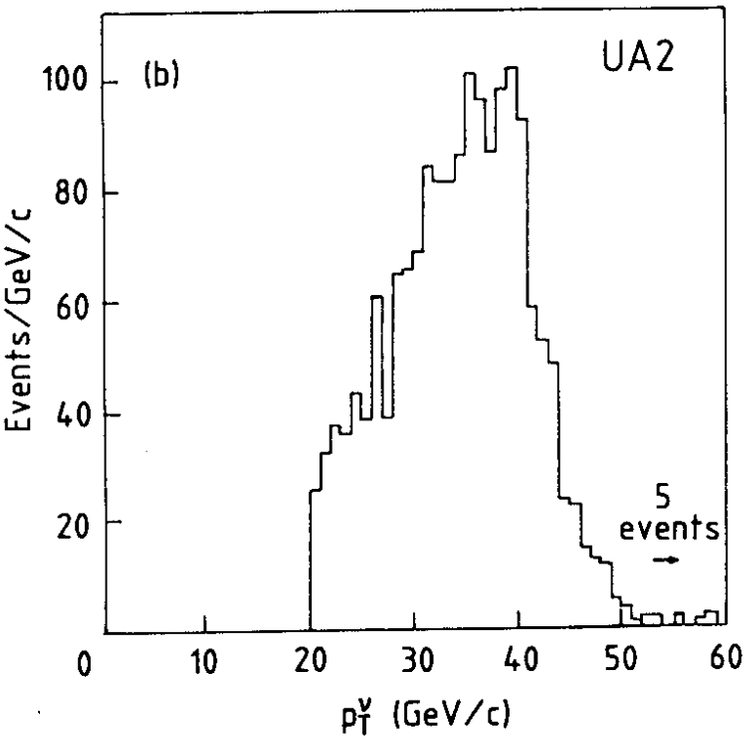
(b)
UA2
Events/GeV/c
100
80
60
40
20
0
10
20
30
40
50
60
5
events
p_T^ν (GeV/c)

Fig. 4

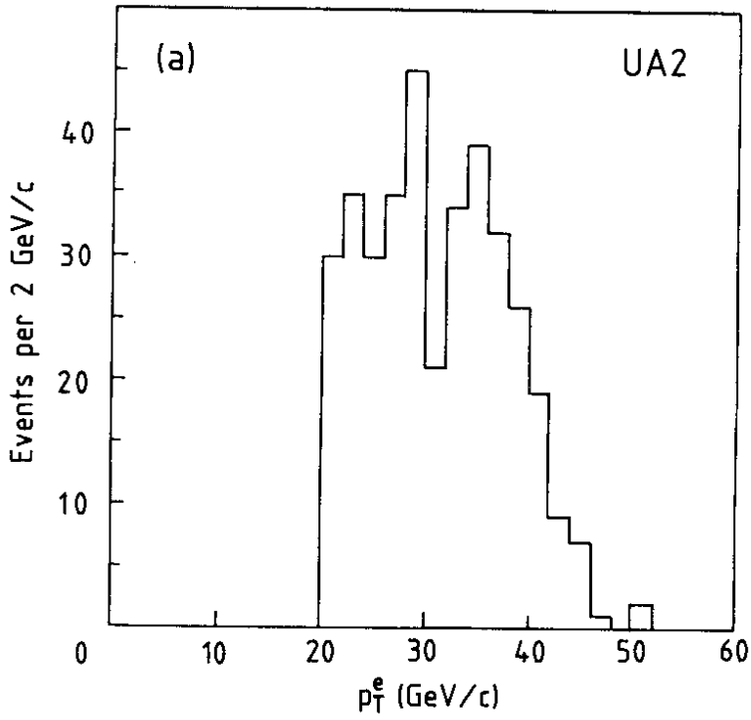
(a)
UA2
Events per 2 GeV/c
0
10
20
30
40
50
60
p_T^e (GeV/c)

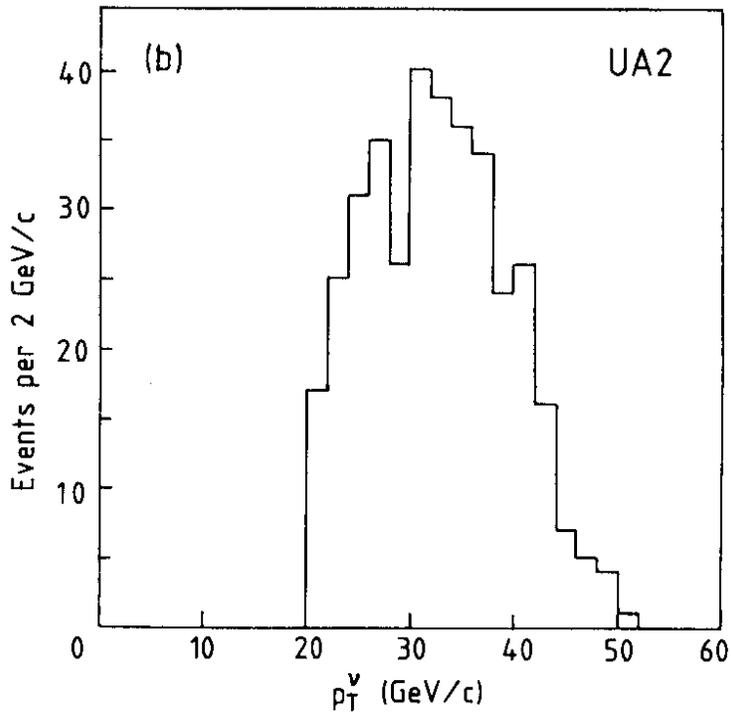
(b)
UA2
Events per 2 GeV/c
0
10
20
30
40
50
60
p_T^ν (GeV/c)

Fig. 5

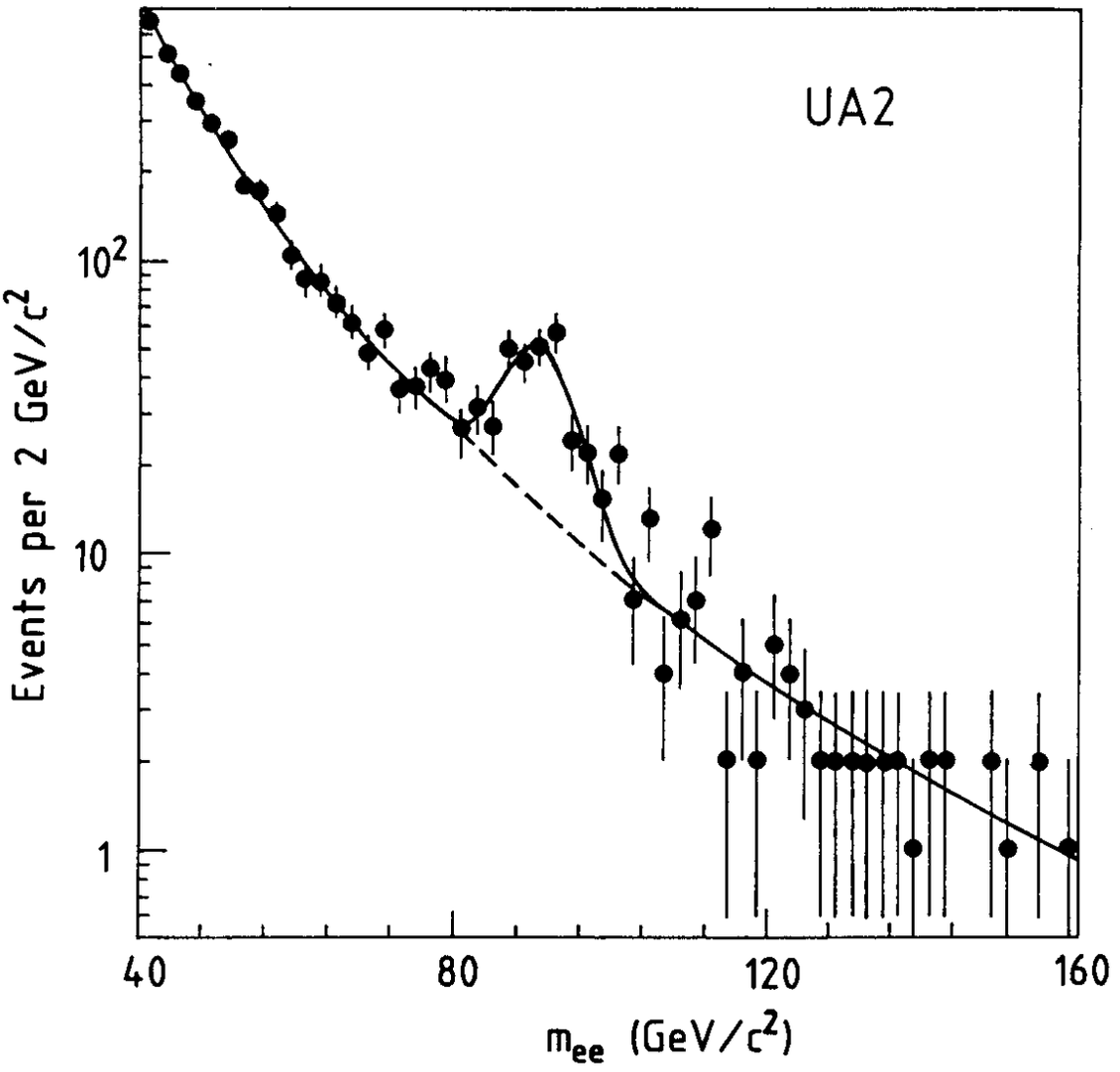

Fig. 6

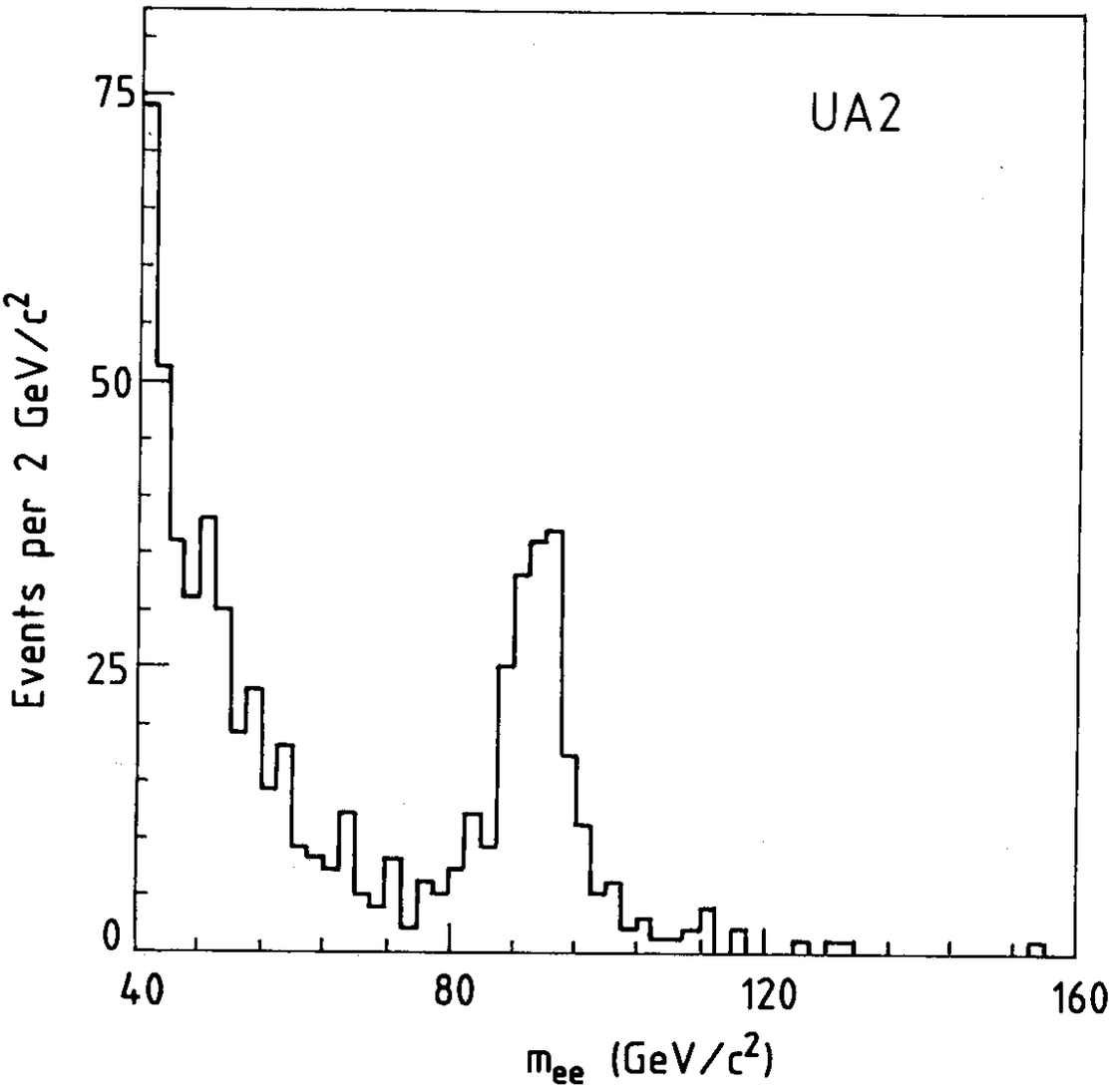

Fig. 7

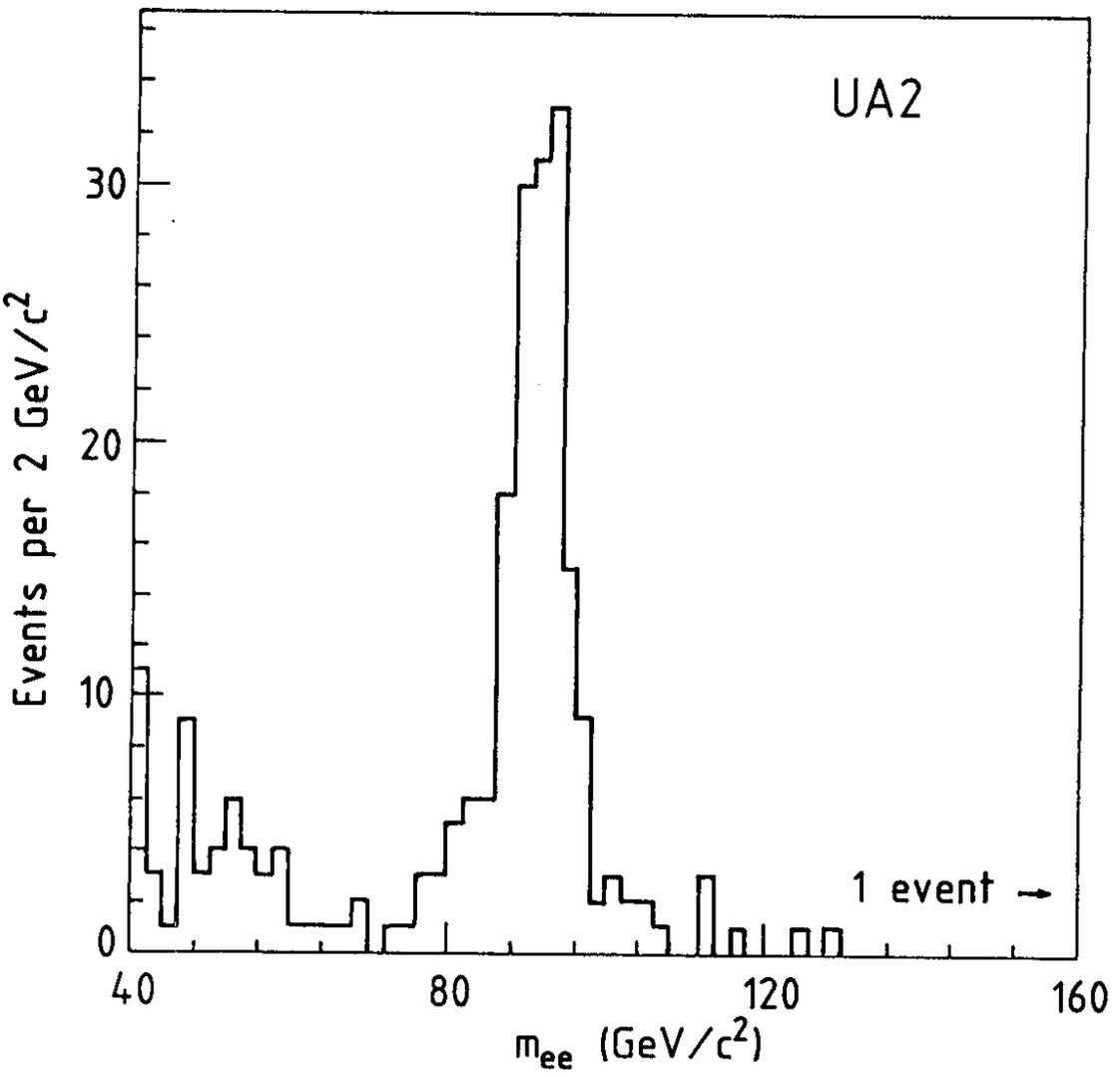

Fig. 8

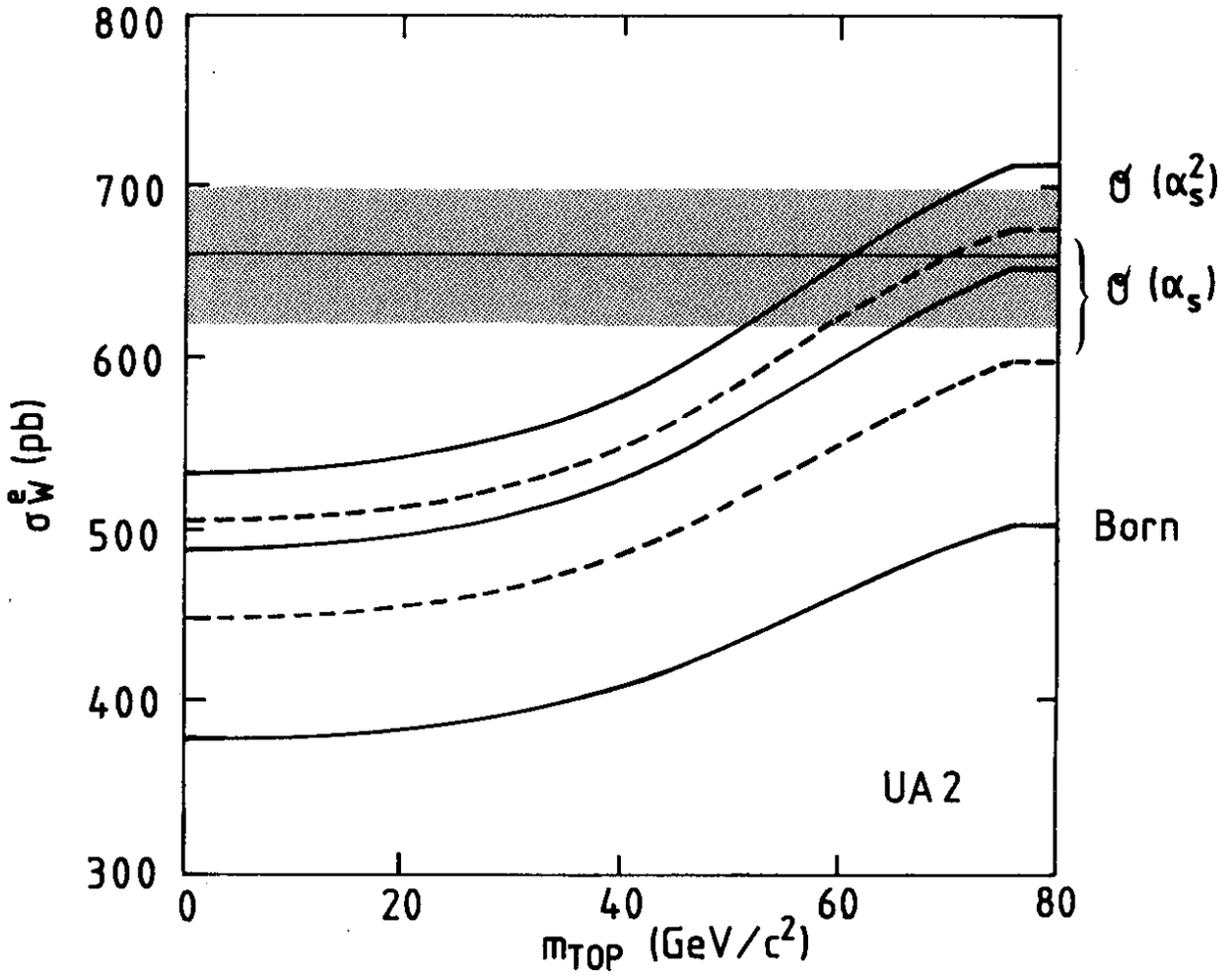
800
700
600
500
400
300
0
20
40
60
80
σ_W^e (pb)
m_{TOP} (GeV/c^2)
$\sigma(\alpha_s^2)$
$\sigma(\alpha_s)$
Born
UA 2

Fig. 9

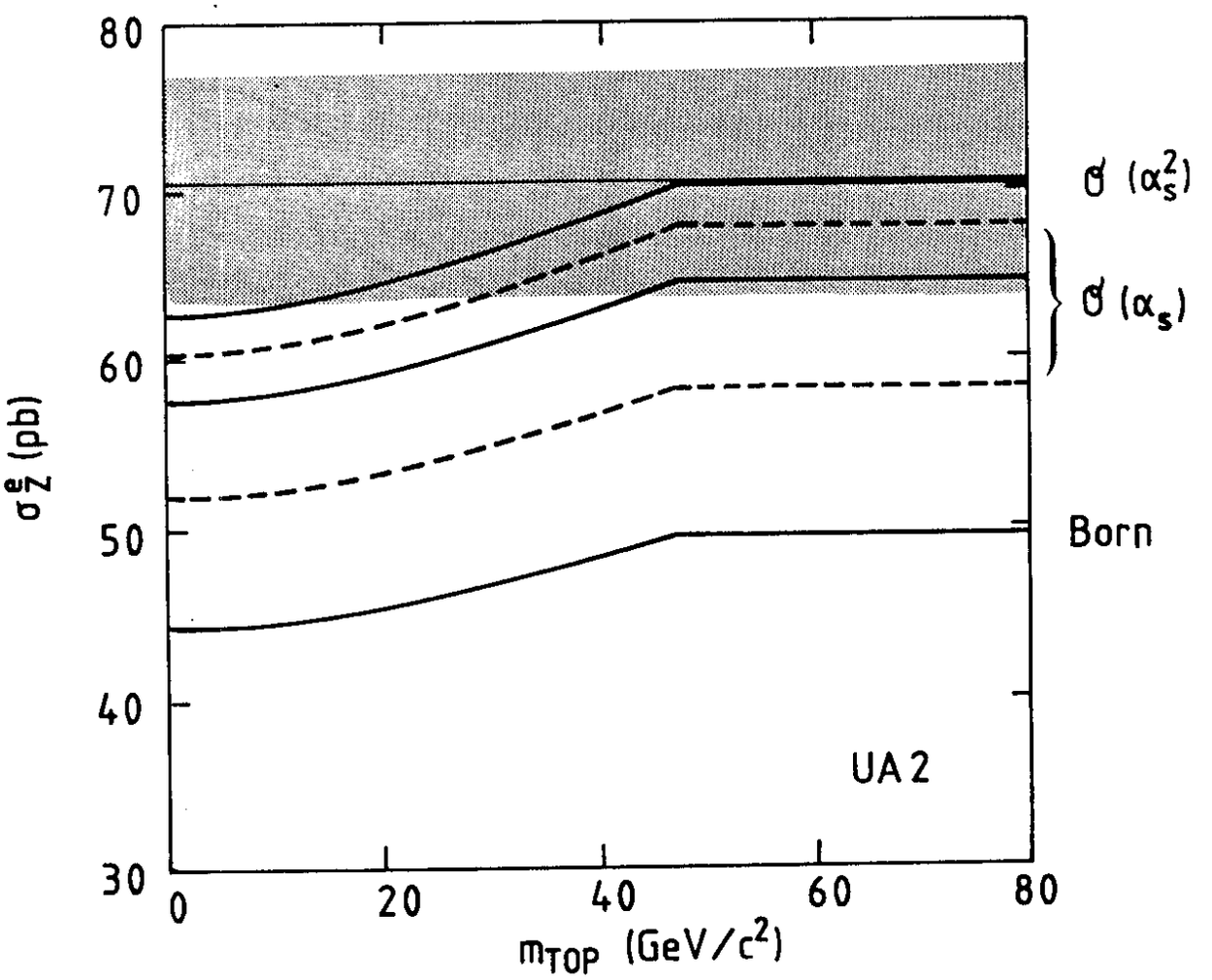
80
70
60
50
40
30
0
20
40
60
80
σ_Z^e (pb)
m_{TOP} (GeV/c^2)
$\sigma(\alpha_s^2)$
$\sigma(\alpha_s)$
Born
UA2

Fig. 10

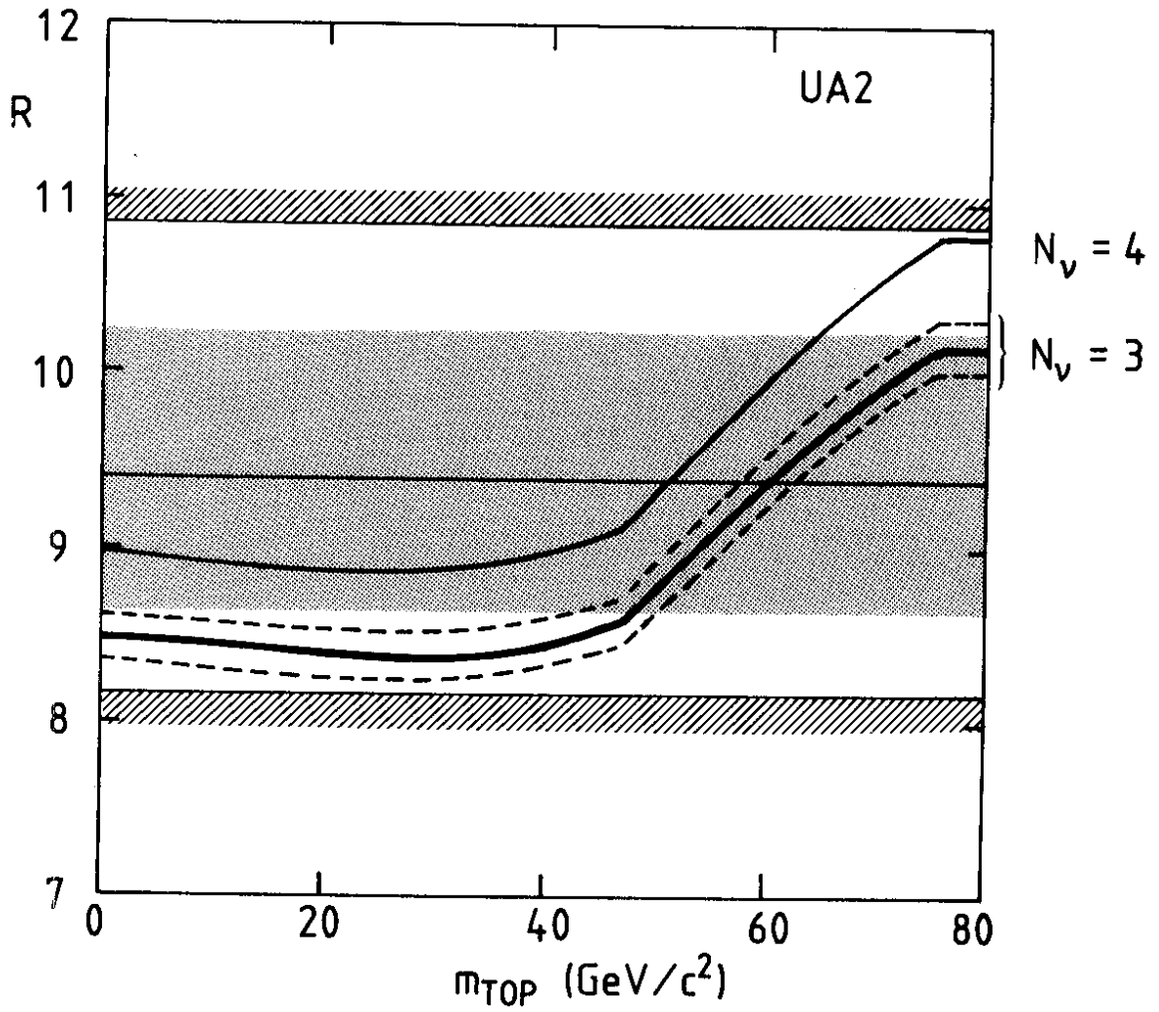

Fig. 11